Supporting Information for
"Mineral dust instantaneous radiative forcing in the Arctic"

A. Kylling[1], C. D. Groot Zwaaftink[1], Andreas Stohl[1]

[1]NILU-Norwegian Institute for Air Research

Contents

S1 Liquid water and ice clouds

The radiative transfer calculations included ice and water clouds, which were taken from European Centre for Medium-Range Weather Forecast (ECMWF) operational analysis data. Water droplet effective radius was calculated with the parameterisation of *Martin et al.* [1994] and the optical properties of the water clouds were calculated from Mie theory. The ice particles were assumed to be solid columns. Their effective radius was calculated from the parameterisation of *Wyser* [1998] and *McFarquhar et al.* [2003]. The optical properties were taken from *Yang et al.* [2005] and processed as described by *Key et al.* [2002]. Examples of vertically integrated ECMWF water and ice cloud column densities are shown in Fig. S1b and Fig. S1c, respectively.

The vertical resolution of the radiative transfer simulations was dictated by the vertical resolution of the ice and water cloud fields from ECMWF and mineral dust fields from *Groot Zwaaftink et al.* [2016]. Typically around 106 layers were used.

Corresponding author: Arve Kylling, arve.kylling@nilu.no

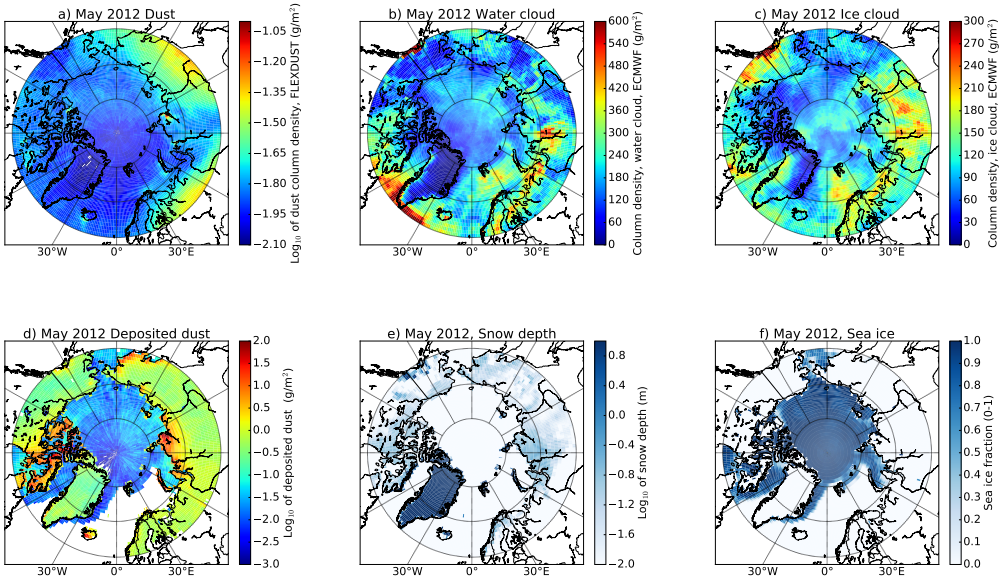

Figure S1. Examples of monthly averaged vertically integrated dust (a), water cloud (b) and ice cloud (c) amounts for May 2012. The vertically resolved concentrations of these quantities were input to the radiative transfer model. (d) The dust deposited on snow covered land and sea ice. (e) Snow depth on land. Note that snow depths much larger than 10 m are present and that the 10 m maximum value was chosen only for clarity of presentation. (f) Sea ice fraction.

S2 Surface albedo

For snow free surfaces the surface albedo was taken from ECMWF analysis data. For snow covered land surfaces and sea ice, the albedo was calculated using the SNICAR model [*Flanner et al.*, 2007, 2009]. For land surfaces the snow water equivalent data from ECMWF was used to determine whether the ground was snow covered or not. The snow water equivalent (d_{SWE}) was converted to snow depth (d_S) needed by SNICAR as follows

$$d_S = d_{SWE}\rho_{liquid}/\rho_{solid} \tag{1}$$

where ρ_{solid} and ρ_{liquid} are the densities of snow (from ECMWF) and water, respectively. An example of the snow depth is shown in Fig. S1e for May 2012.

Ocean covered by sea ice was identified from ECMWF data. It was assumed that all sea ice was covered with a 20 cm thick snow layer with density of 290 kg/m^3. While the albedo of late season bare ice is certainly different from snow covered ice we justify this approach by noting that: 1) The dust IRF is largest in April-May when the sea ice is expected to be snow covered; and 2) The dust IRF is smaller over ocean than over land. The choices of snow layer thickness and density were adopted from *Kern et al.* [2015]. The sea ice fraction was included by reducing the albedo by the sea ice fraction. An example of the sea ice fraction is shown in Fig. S1f for May 2012. For the year studied, 2012, the Arctic sea ice extent was at its minimum (https://www.climate.gov/news-features/understanding-climate/climate-change-minimum-arctic-sea-ice-extent). In another year with more sea ice, dust IRF may be larger.

The radiation penetration depth of snow depends on wavelength and snow grain size [see Table 2 in *Stamnes et al.*, 2007]. A conservative point of view is that the underlying surface has little impact on the reflected radiation if the snow layer is thicker than about 20 cm [*Flanner et al.*, 2009]. For thinner snow layers the albedo of the underlying surface may impact the amount of reflected radiation. SNICAR allows the albedo of the underlying surface to be specified in two wavelength intervals, 0.3-0.7 μm and 0.7-5.0 μm. For snow covered land surfaces an underlying surface albedo of 0.2 (0.4) was used for wavelengths between 0.3-0.7 μm (between 0.7-5.0 μm). These choices were made based on data presented by *Varotsos et al.* [2014]. For the ocean constant albedo values of 0.04 between 0.3-0.7 μm, and 0.02 between 0.7-5.0 μm, were used if the ocean was covered by snow and sea ice. In the infrared, the emissivity was set to one.

In addition to dust concentration in the atmosphere, *Groot Zwaaftink et al.* [2016] also reported deposited dust. The amount of deposited dust is shown for each month in Fig. S2. Note that for each pixel this is the cumulative deposited dust as long as there is snow on the surface. If the snow disappears the amount of deposited dust is nulled. Deposited dust is accumulated again when snow returns.

S2.1 Snow grain size, snow layer thickness, snow density and underlying surface albedo

The albedo of snow depends, amongst other properties, on the snow grain size [*Wiscombe and Warren*, 1980], and snow grain effective radius is one of the inputs to the SNICAR model. No global monthly averaged snow grain size data are readily available. However, *Hori et al.* [2007] presented maps of snow grain size for the Arctic. Their method to derive the effective grain size is described by *Stamnes et al.* [2007] and a validation is presented by *Aoki et al.* [2007]. The retrieved grain size depends on radiation penetration depth which is wavelength dependent [see e.g. *Stamnes et al.*, 2007]. Also, the effective grain size is different from the vertically varying grain size. An example of dust in snow IRF as a function of effective snow grain radius is shown in Fig. S3. Dust concentrations of 0.19, 0.73, 8.71, and 82.49 ppm in SNICAR dust bins 1(0.1-1.0 μm diameter), 2 (1.0-2.5 μm) , 3 (2.5-5.0 μm) and 4 (5.0-10.0 μm) respectively, were used. Both cloudy and cloudless results are presented for the bottom of the atmosphere or surface (BOA, red lines) and top of the atmosphere (TOA, blue lines). Comparing cloudy cases (a and b in Fig. S3) with the cloudless simulation, we conclude that the presence of clouds reduces the sensitivity of dust IRF to the effective snow grain radius (Fig. S3). Based on these results, the maps of *Hori et al.* [2007], and the lack of spatio-temporally resolved snow grain size data we adopt a constant snow grain radius of 200 μm.

Changing the snow density, snow thickness and underlying albedo also effect the IRF due to dust deposited on snow. This is demonstrated for cloudless conditions in Fig. S4 which shows the IRF as a function of snow layer thickness. For snow thickness above about 20-30 cm the snow density, snow thickness and underlying albedo have little effect on the IRF.

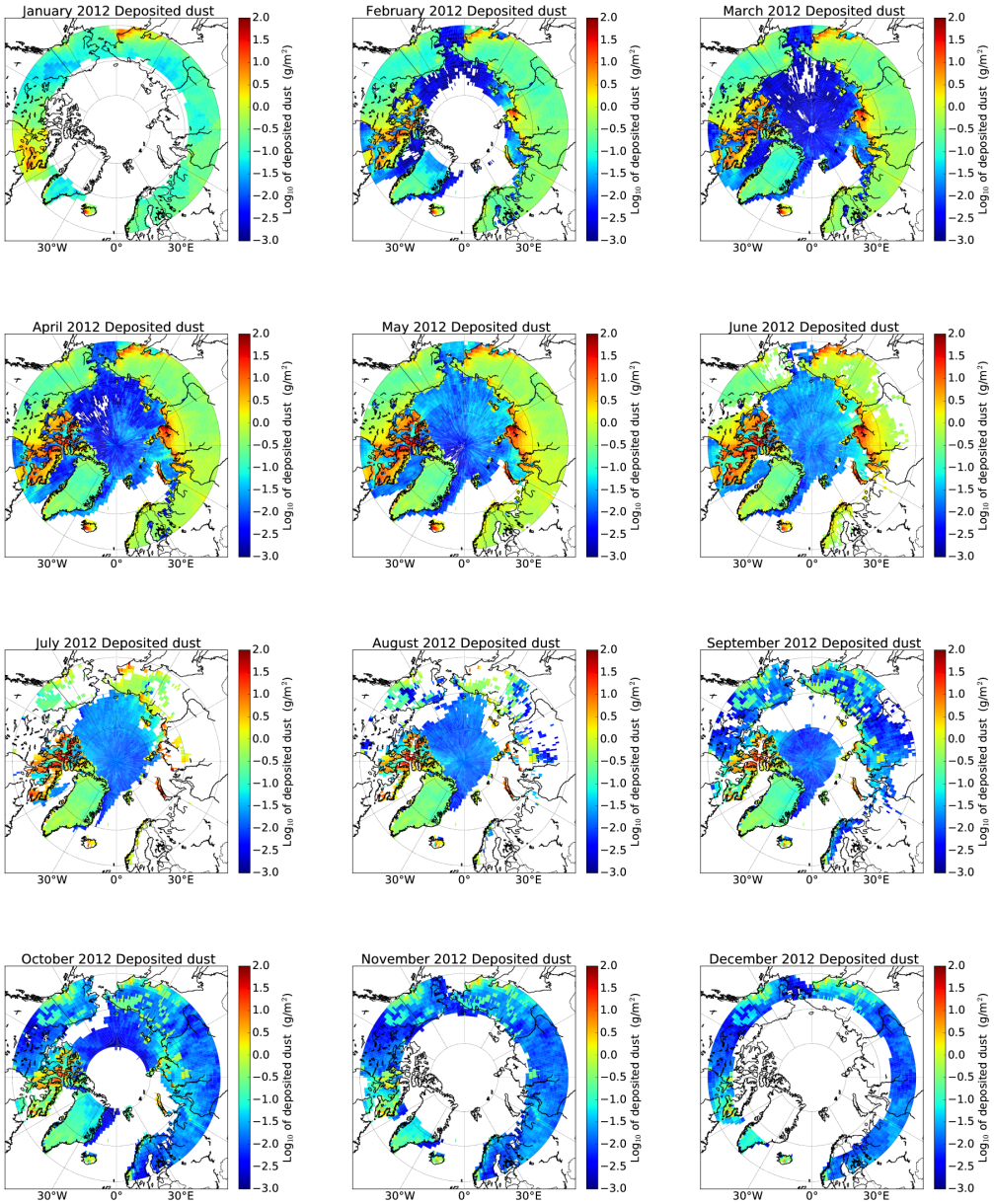

Figure S2. The amount of deposited dust on snow covered land and sea ice throughout 2012. Values are not shown when the solar zenith angle is larger than 88°.

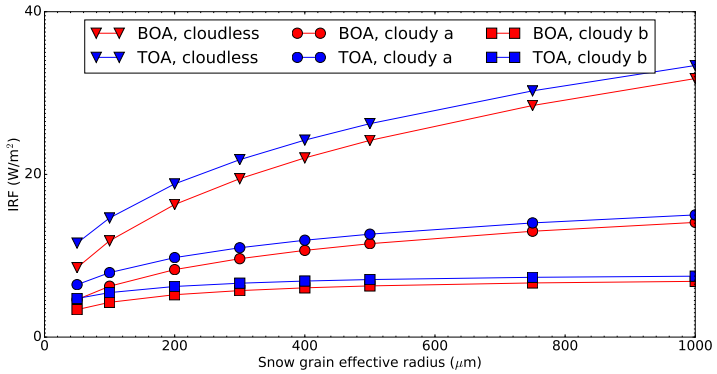

Figure S3. The instantaneous radiative forcing due to dust shown as a function of effective snow grain size for cloudless conditions and two cloudy cases. The cloudy cases have visible optical depths of about 16 (case a) and 63 (case b). The snow depth is 2 m and the snow density 200 kg/m^3. The atmospheric dust load is 0.05 g/m^2. The calculations are representative for a latitude of 75° in mid-May.

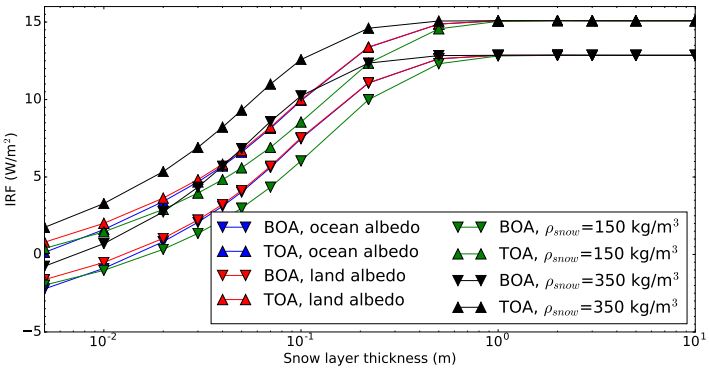

Figure S4. The instantaneous radiative forcing (IRF) due to dust shown as a function of snow thickness for cloudless conditions. Two different albedos for the underlying surface are considered (blue and red lines). The ocean and land albedos are as given in section S2. The snow density (ρ_{snow}) is 200 kg/m^3 for the blue and red lines and 150 kg/m^3 for the green lines and 350 kg/m^3 for the black lines. The deposited dust and atmospheric dust load are as in Fig. S3. Results are shown for the BOA (down-pointing triangle) and TOA (up-pointing triangle). The calculations are representative for a latitude of 75° in mid-May.

S3 Mineral dust optical properties

An example of the simulated dust column from *Groot Zwaaftink et al.* [2016] is shown in Fig. S1a. The dust is the sum of transported dust from all source regions. For the IRF calculation the same optical properties were used for dust from all sources. In reality the optical properties of dust from different regions differ and this will influence the total dust IRF as well as the relative contributions from different source regions. However, this has not been assessed in this study.

The dust optical properties were taken from the the SNICAR model [*Flanner et al.*, 2007, 2009]. The dust optical properties vary with size distribution, composition and other factors. We used the same dust optical properties in the atmosphere and the snow. In addition we performed simulations where the atmospheric dust optical properties were taken from the Optical properties of aerosols and clouds (OPAC) database [*Hess et al.*, 1998]. The OPAC dust optical properties increased the IRF by about a factor 2. The abundance of iron oxides largely determines the absorption by dust in the shortwave. *Balkanski et al.* [2007] constrained the iron oxides abundance in dust using AERONET retrieved refractive indexes. They found the dust less absorbing than in many previous studies that used dust optical properties similar to those in the OPAC database. We also note that according to *Albani et al.* [2014] the OPAC aerosol model "yield optical properties that give dust the tendency to be too absorbing compared to observations." Our choice of dust optical properties are in-line with those of *Balkanski et al.* [2007]. We do acknowledge the need for further measurement of optical properties of dust from different regions.

Dust particles are generally non-spherical, but are often assumed to be spherical in radiative transfer calculations. The impact of the spherical particle assumption for climate energy budget calculations is not a settled issue. *Nousiainen* [2009] states that “contrary to the popular belief, the use of Mie spheres is a major source of error even in radiation-budget consideration”. This was supported by calculations by *Yi et al.* [2011]. However, *Räisänen et al.* [2013] concluded that the spherical particle assumption had negligible effects on climate simulations, a result supported by IRF calculations by *Wang et al.* [2013]. Here we use spherical particles and calculate their optical properties from Mie theory.

S4 Instantaneous radiative forcing (IRF)

Longwave (thermal)and shortwave (solar) irradiances (E) were calculated using the uvspec model from the libRadtran software package [*Mayer and Kylling*, 2005; *Emde et al.*, 2016]. The independent column approximation was adopted and the radiative transfer equation solved using an improved version of DISORT [*Stamnes et al.*, 1988; *Buras et al.*, 2011] in pseudo-spherical geometry [*Dahlback and Stamnes*, 1991] with absorption by gases was taken from the *Fu and Liou* [1992] parameterization. Six streams were used to account for the non-isotropic phase function of the dust and cloud particles, while keeping computational cost at a manageable level. To avoid numerical problems, solar calculations were not made for solar zenith angles larger than 88°. For IRF calculations the omission of solar radiation at these large solar zenith angles is negligible.

The IRF was calculated as:

$$IRF = E^{f}_{\text{net}} - E^{bg}_{\text{net}} \tag{2}$$

where the f and bg superscripts denote quantities with the forcing agent included and background conditions without the forcing agent, respectively. Furthermore

$$E_{\text{net}} = E^{+} - E^{-} = E^{+}_{\text{solar}} + E^{+}_{\text{thermal}} - (E^{-}_{\text{solar}} + E^{-}_{\text{thermal}}), \tag{3}$$

where E^{+} (E^{-}) denotes upwelling (downwelling) irradiance at a given level of the atmosphere. Subscripts "solar" and "thermal" refer to the shortwave and longwave part of the spectrum. We note that the thermal part is only affected by the atmospheric dust load as we have not included any emissivity change in the thermal due to deposited dust. The IRF was calculated at the bottom (BOA) or surface, and top (TOA) of the atmosphere.

S5 IRF maps

Monthly averaged dust fields for the year 2012 were taken from *Groot Zwaaftink et al.* [2016] and monthly averaged cloud and surface data were calculated from ECMWF data fields. The IRF was calculated for the middle of the month. Examples of IRF maps for May 2012 are shown in Fig. S5 for BOA and TOA and with and without deposited dust. For this month, excluding the radiative effect of deposited dust (Figs. S5a and S5c), the TOA (BOA) IRF varies between 0.086 and 1.095 W/m^2 (-0.223 and 0.255). Including deposited dust (Figs. S5b and S5d), the TOA (BOA) IRF is more inhomogeneous and varies between -0.060 and 14.196 W/m^2 (-0.451 and 14.709). The effect of deposited dust is largest where there is

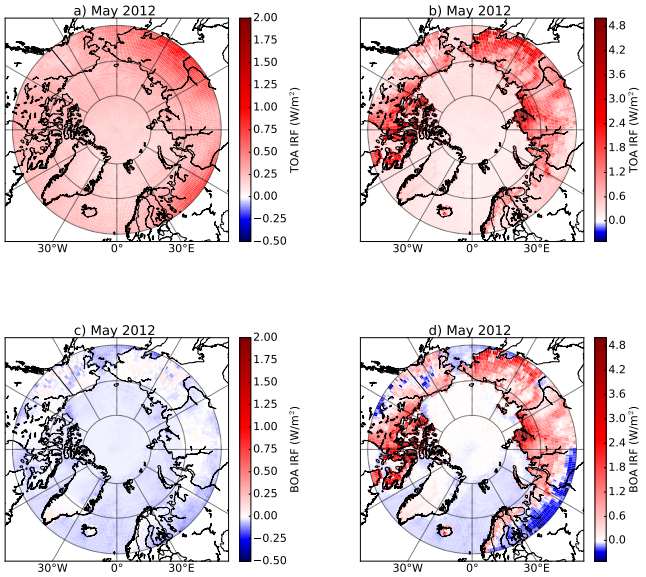

Figure S5. The monthly averaged TOA (a) and BOA (c) dust IRF for May 2012, including water and ice clouds and dust in the atmosphere, but no dust deposited on the surface. Corresponding values including dust deposited on the surface are shown in panels (b) and (d). Note differences in color bar scale.

deposited dust on snow covered ground (Fig. S1d) and cloud coverage is small (Figs. S1b and S1c). From maps such as those in Fig. S5, area averaged IRF values were calculated.

S6 IRF as a function of Arctic definition

In Fig. S6 we show how the yearly averaged TOA and BOA IRF changes as the southern latitude delimiting the Arctic, is moved northwards. The TOA IRF levels off for latitude limits above about 75°N while the BOA IRF peaks and then drops for larger latitude limits. This different behavior is due to TOA IRF being largely influenced by airborne dust above clouds, while BOA IRF is comparatively more influenced by surface dust. Surface dust concentrations and dust deposition decrease towards higher latitudes.

S7 IRF uncertainty

To make a full uncertainty estimate for the IRF would require systematic varying all parameters affecting the IRF for the period under study. This is beyond the scope of the present work. However, below we present a simplified IRF uncertainty estimate.

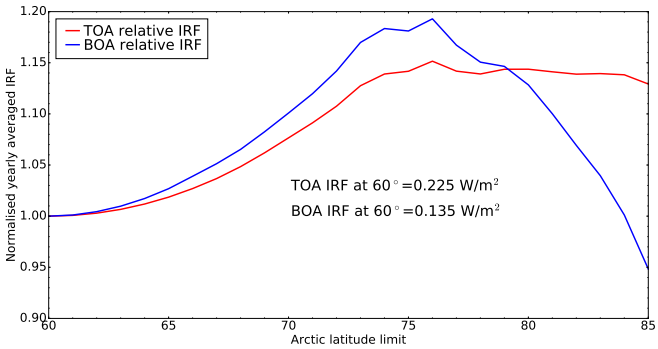

Figure S6. The yearly averaged TOA (red) and BOA (blue) dust IRF as a function of the lower latitude limit defining the Artic.

The IRF will change with the amount of dust in the atmosphere and the deposited dust. In Fig. S7 is shown the percent change in IRF with the percent change of both dust in the atmosphere and deposited dust. From Fig. S7 we estimate that a ±50% change in atmospheric dust load and dust deposition gives about a ±30% change in the IRF. As shown in Fig. S3, the IRF changes with snow grain size . We adopted a value of 200 μm for the snow grain size. The change in IRF with snow grain size depends on whether clouds are present or not. Assuming an uncertainty of ±100 μm for the snow grain size, we estimate an IRF uncertainty that covers both cloudy and cloudless skies to be about 20%. For thin snow layers the IRF is sensitive to the snow thickness as shown in Fig. S4. Assuming an uncertainty in the snow depth of ±30% the corresponding IRF uncertainty is estimated to about ±25%. The dust optical properties will vary with dust origin. In lack of data we used the same dust optical properties all over. Based on simulations made with more absorbing aerosols in the atmosphere, we assign an IRF uncertainty of ±50% due to the uncertainty in the dust optical properties.

Adding the square of all uncertainty estimates and taking the root gives an overall uncertainty of ±67% for the IRF. Note that this uncertainty does not include uncertainties due to the water and ice clouds, the assumption of 1D radiative transfer, surface tilt, and dust shape.

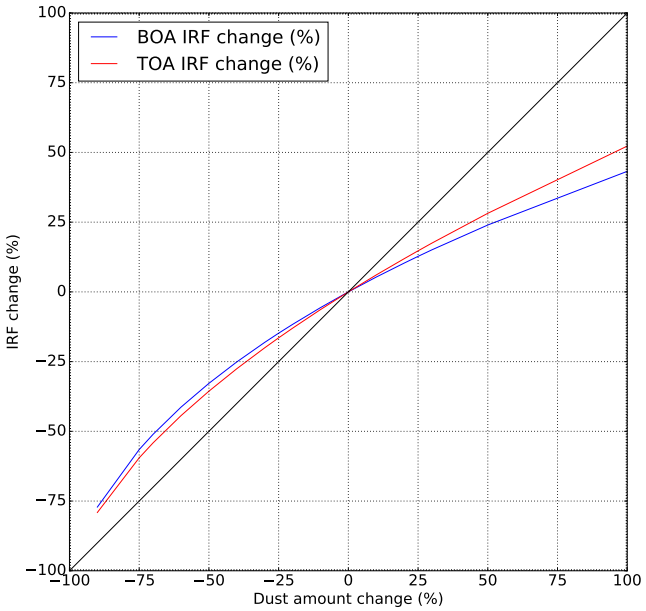

Figure S7. The % change TOA (red) and BOA (blue) dust IRF as a function of % in atmospheric dust load and deposited dust. The calculations are representative for a latitude of 75° in mid-May.

S8 Dust source IRF efficiency

The efficiency of a dust source region to affect the Arctic radiative environment may be estimated by dividing dust IRF by the amount of dust mass emitted in the region and is shown in Fig. S8a,b for the TOA and BOA.

References

Albani, S., N. M. Mahowald, A. T. Perry, R. A. Scanza, C. S. Zender, N. G. Heavens, V. Maggi, J. F. Kok, and B. L. Otto-Bliesner (2014), Improved dust representation in the Community Atmosphere Model, *J. Adv. Model. Earth Syst.*, *6*, 541-570, doi: 10.1002/2013MS000279.

Aoki, T., M. Hori, H. Motoyoshi, T. Tanikawa, A. Hachikubo, K. Sugiura, T. J. Yasunari, R. Storvold, H. A. Eide, K. Stamnes, W. Li, J. Nieke, Y. Nakajima, and F. Takahashi (2007), Adeos-ii/gli snow/ice products - part ii: Validation results using gli and modis data, *Remote Sensing of Environment*, *111*(2-3), 274 – 290, doi: http://dx.doi.org/10.1016/j.rse.2007.02.035, remote Sensing of the Cryosphere Special

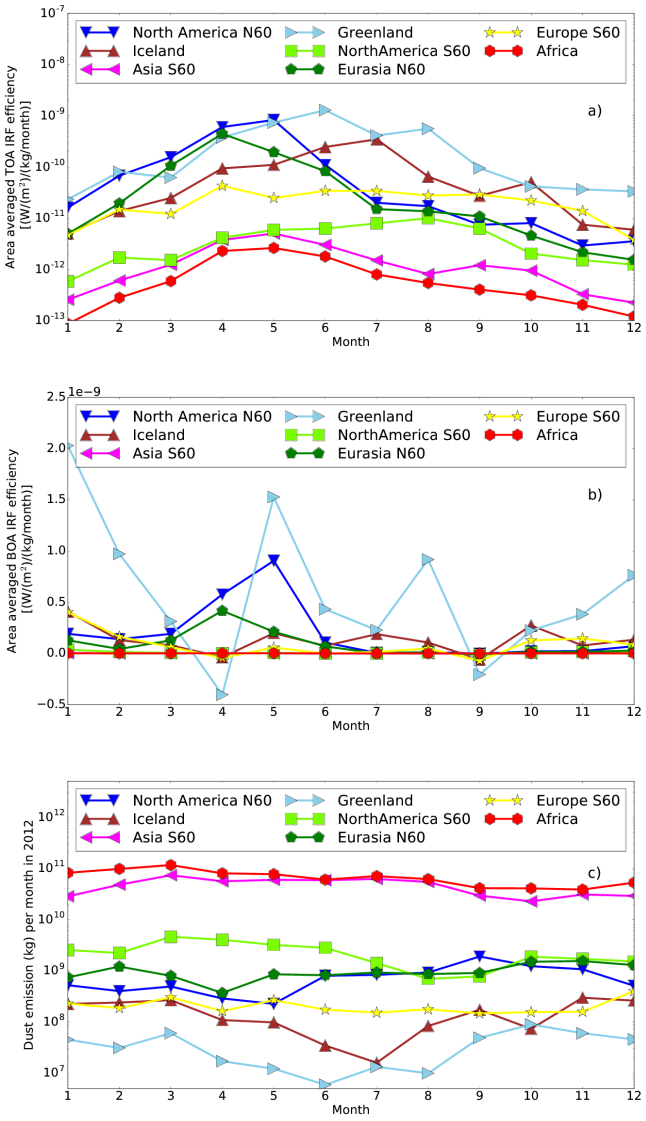

Figure S8. TOA (a) and BOA (b) area averaged dust radiative forcing efficiency (i.e. forcing per kg emitted dust) for 2012 conditions. Note the logarithmic scale on y-axis on TOA plot. (c) Dust emission (kg) per month in 2012 for specific regions.

Issue.

Balkanski, Y., M. Schulz, T. Claquin, and S. Guibert (2007), Reevaluation of mineral aerosol radiative forcings suggests a better agreement with satellite and aeronet data, *Atmospheric Chemistry and Physics*, *7*(1), 81–95, doi:10.5194/acp-7-81-2007.

Buras, R., T. Dowling, and C. Emde (2011), New secondary-scattering correction in DISORT with increased efficiency for forward scattering, *J. Quant. Spectrosc. Radiat. Transfer*, *112*, 2028–2034, doi:10.1016/j.jqsrt.2011.03.019.

Dahlback, A., and K. Stamnes (1991), A new spherical model for computing the radiation field available for photolysis and heating at twilight, *Planet. Space Sci.*, *39*, 671–683.

Emde, C., R. Buras-Schnell, A. Kylling, B. Mayer, J. Gasteiger, U. Hamann, J. Kylling, B. Richter, C. Pause, T. Dowling, and L. Bugliaro (2016), The libradtran software package for radiative transfer calculations (version 2.0.1), *Geoscientific Model Development*, *9*(5), 1647–1672, doi:10.5194/gmd-9-1647-2016.

Flanner, M. G., C. S. Zender, J. T. Randerson, and P. J. Rasch (2007), Present-day climate forcing and response from black carbon in snow, *Journal of Geophysical Research: Atmospheres*, *112*(D11), doi:10.1029/2006JD008003.

Flanner, M. G., C. S. Zender, P. G. Hess, N. M. Mahowald, T. H. Painter, V. Ramanathan, and P. J. Rasch (2009), Springtime warming and reduced snow cover from carbonaceous particles, *Atmospheric Chemistry and Physics*, *9*(7), 2481–2497, doi:10.5194/acp-9-2481-2009.

Fu, Q., and K. N. Liou (1992), On the correlated k-distribution method for radiative transfer in nonhomogeneous atmospheres, *J. Atmos. Sci.*, *49*, 2139–2156.

Groot Zwaaftink, C. D., H. Grythe, H. Skov, and A. Stohl (2016), Substantial contribution of northern high-latitude sources to mineral dust in the arctic, *Journal of Geophysical Research: Atmospheres*, *121*(22), 13,678–13,697, doi:10.1002/2016JD025482, 2016JD025482.

Hess, M., P. Koepke, and I. Schult (1998), Optical properties of aerosols and clouds: The software package OPAC, *Bulletin of the American Meteorological Society*, *79*, 831–844.

Hori, M., T. Aoki, K. Stamnes, and W. Li (2007), Adeos-ii/gli snow/ice products - part iii: Retrieved results, *Remote Sensing of Environment*, *111*(2-3), 291 – 336, doi: http://dx.doi.org/10.1016/j.rse.2007.01.025, remote Sensing of the Cryosphere Special Issue.

Kern, S., K. Khvorostovsky, H. Skourup, E. Rinne, Z. S. Parsakhoo, V. Djepa, P. Wadhams, and S. Sandven (2015), The impact of snow depth, snow density and ice density on sea ice thickness retrieval from satellite radar altimetry: results from the esa-cci sea ice ecv project round robin exercise, *The Cryosphere*, *9*(1), 37–52, doi:10.5194/tc-9-37-2015.

Key, J. R., P. Yang, B. A. Baum, and S. L. Nasiri (2002), Parameterization of shortwave ice cloud optical properties for various particle habits, *J. Geophys. Res.*, *107*(D13), AAC 7–1–AAC 7–10, doi:doi:10.1029/2001JD000742.

Marticorena, B., and G. Bergametti (1995), Modeling the atmospheric dust cycle: 1. design of a soil-derived dust emission scheme, *Journal of Geophysical Research: Atmospheres*, *100*(D8), 16,415–16,430, doi:10.1029/95JD00690.

Martin, G. M., D. W. Johnson, and A. Spice (1994), The measurement and parameterization of effective radius of droplets in warm stratocumulus clouds, *J. Atmos. Sci.*, *51*, 1823–1842.

Mayer, B., and A. Kylling (2005), Technical note: the libRadtran software package for radiative transfer calculations-description and examples of use, *Atmos. Chem. Phys.*, *5*, 1855–1877.

McFarquhar, G. M., S. Iacobellis, and R. C. J. Somerville (2003), SCM simulations of tropical ice clouds using observationally based parameterizations of microphysics, *J. of Climate*, *16*, 1643–1664.

Nousiainen, T. (2009), Optical modeling of mineral dust particles: A review, *Journal of Quantitative Spectroscopy and Radiative Transfer*, *110*(14-16), 1261 – 1279, doi: http://dx.doi.org/10.1016/j.jqsrt.2009.03.002, xI Conference on Electromagnetic and Light Scattering by Non-Spherical Particles: 2008.

Räisänen, P., P. Haapanala, C. E. Chung, M. Kahnert, R. Makkonen, J. Tonttila, and T. Nousiainen (2013), Impact of dust particle non-sphericity on climate simulations, *Quarterly Journal of the Royal Meteorological Society*, *139*(677), 2222–2232, doi:10.1002/qj.2084.

Stamnes, K., S.-C. Tsay, W. Wiscombe, and K. Jayaweera (1988), Numerically stable algorithm for discrete–ordinate–method radiative transfer in multiple scattering and emitting layered media, *Appl. Opt.*, *27*, 2502–2509.

Stamnes, K., W. Li, H. Eide, T. Aoki, M. Hori, and R. Storvold (2007), Adeos-ii/gli snow/ice products – part i: Scientific basis, *Remote Sensing of Environment*, *111*(2–3), 258 – 273, doi:http://dx.doi.org/10.1016/j.rse.2007.03.023, remote Sensing of the Cryosphere Special Issue.

Varotsos, C. A., I. N. Melnikova, A. P. Cracknell, C. Tzanis, and A. V. Vasilyev (2014), New spectral functions of the near-ground albedo derived from aircraft diffraction spectrometer observations, *Atmospheric Chemistry and Physics*, *14*(13), 6953–6965, doi:10.5194/acp-14-6953-2014.

Wang, Z., H. Zhang, X. Jing, and X. Wei (2013), Effect of non-spherical dust aerosol on its direct radiative forcing, *Atmospheric Research*, *120-121*, 112 – 126, doi: http://dx.doi.org/10.1016/j.atmosres.2012.08.006.

Wiscombe, W. J., and S. G. Warren (1980), A model for the spectral albedo of snow, I, Pure snow, *J. Atmos. Sci.*, *37*, 2712–2733.

Wyser, K. (1998), The effective radius in ice clouds, *J. of Climate*, *11*, 1793–1802.

Yang, P., H. Wei, H.-L. Huang, B. Baum, Y. X. Hu, G. W. Kattawar, M. I. Mishchenko, and Q. Fu (2005), Scattering and absorption property database for nonspherical ice particles in the near- through far-infrared spectral region, *Appl. Opt.*, *44*, 5512–5523.

Yi, B., C. N. Hsu, P. Yang, and S.-C. Tsay (2011), Radiative transfer simulation of dust-like aerosols: Uncertainties from particle shape and refractive index, *Journal of Aerosol Science*, *42*(10), 631–644, doi:http://dx.doi.org/10.1016/j.jaerosci.2011.06.008.